Journal Pre-proof

Chemical, optical and transport characterization of ALD modified nanoporous alumina based structures

A.L. Cuevas, M[a]. Valle Martínez de Yuso, L. Gelde, A.S. González, V. Vega, V.M. Prida, J. Benavente

PII: S1226-086X(20)30347-6

DOI: https://doi.org/10.1016/j.jiec.2020.07.048

Reference: JIEC 5164

To appear in: *Journal of Industrial and Engineering Chemistry*

Received Date: 23 May 2020

Revised Date: 20 July 2020

Accepted Date: 25 July 2020

Please cite this article as: { doi: https://doi.org/

Chemical, optical and transport characterization of ALD modified nanoporous alumina based structures

A. L. Cuevas[†], Mª. Valle Martínez de Yuso[‡], L. Gelde[§], A.S. González[$], V. Vega[#,*], V. M. Prida[$,*], J. Benavente[§]

[†] Unidad de Nanotecnología, SCBI Centro, Universidad de Málaga, E-29071 Málaga, Spain.
[‡] Servicios Centrales de Investigación, Universidad de Málaga, E-29071 Málaga, Spain.
[§] Departamento de Física Aplicada I, Facultad de Ciencias, Universidad de Málaga, E-29071 Málaga, Spain.

[$] Departamento de Física, Facultad de Ciencias, Universidad de Oviedo, E-33007 Oviedo, Spain.
[#] Laboratorio de Membranas Nanoporosas, Servicios Científico-Técnicos, Universidad de Oviedo, E-33006 Oviedo, Spain.

Graphical abstract

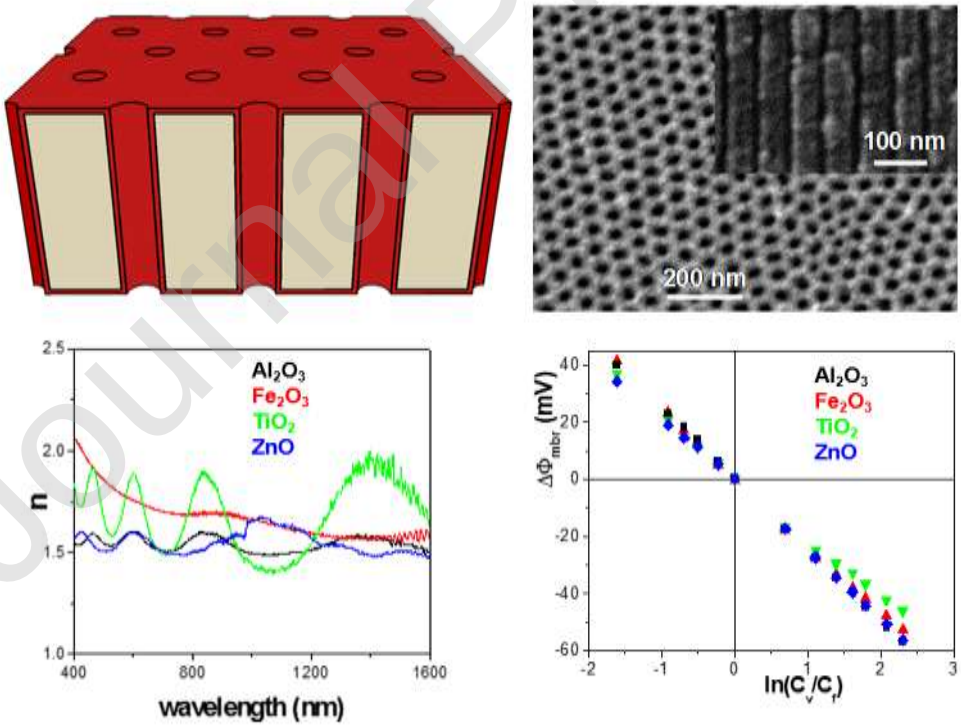

ABSTRACT

Nanoporous alumina-based structures (NPA-bSs) obtained by anodization of aluminum in sulfuric acid medium were coated by Atomic Layer Deposition (ALD) of a thin conformal layer of different functional oxides (Al_2O_3, TiO_2, Fe_2O_3 or ZnO), leading to samples with similar geometrical parameters but different surface materials. Morphological characterization of the NPA-bSs confirms a reduction of about 35% in pore size associated to the presence of the oxides of interest, while chemical surface analysis permits the estimation of cover layer purity and thickness. Additionally, ALD functionalization also modifies optical (band-gap, refractive index and dielectric constant) according to transmittance and spectroscopic ellipsometry results for visible and near-infrared regions, as well as electrolyte diffusive transport parameters (effective fixed charge, ion transport numbers or ionic permselectivity) of the NPA-bSs, both of which are dependent on the nature of the coating layer. Therefore, the suitability of ALD technique for geometrical and functional modification of nanoporous structures is demonstrated, thus broadening the potential application of these NPA-bSs platforms to optical sensing, nanophotonics, biosensing, microfluidics or drug delivery applications.

Key words: Nanoporous alumina, ALD coating, spectroscopic ellipsometry, transmittance, ionic transport.

1. Introduction

Nanoporous materials synthesized by electrochemical techniques are systems of great interest due to their practically ideal porous morphology with applications as membranes (for nanofiltration or drug delivery), nanofluidics, sensors (chemical and/or bio-sensors), nanoemulsions fabrication or optical devices [1-10]. Additionally, to ensure the efficiency in most of these processes, nanoporous structures need to exhibit specific characteristics such as rigidity and material stability (both chemical and thermal) to prevent degradation in case of cleaning protocols, or the possibility of surface modification to increase ions/solutes selectivity, while high specific surface area to volume ratio is a significant characteristic in the case of analytical devices, since it allows the enhancement of optical signals. Among other materials, nanoporous alumina structures (NPASs) prepared by anodization of aluminum foils exhibit parallel cylindrical straight pores with radius between 10-200 nm, inter-pore distance between

65 and 500 nm as well as good chemical and thermal stability, biocompatibility, adequate hardness and large specific surface area [11-14]. Moreover, the possibility of easy pore radii and surface material modifications by different techniques such as infiltration followed by thermal annealing, dip coating, chemical vapour deposition or atomic layer deposition, makes of NPASs excellent substrates for developing new selective membranes or nanostructures for optical, biothechnological or analytical devices [15-17].

In fact, geometrical and surface pore-wall material modifications of patterned nanoporous alumina membranes by atomic layer deposition (ALD) technique has already been reported in the literature as a way to provide to nanoporous alumina-based structures (NPA-bSs) particular physical and chemical characteristics (pore size and porosity, reflectivity, hydrophilicity/hydrophobicity, photoluminescence character, selectivity toward specific molecules/ions…) [18-22]. ALD is a surface modification method used to deposit thin and conformal layers that provide precise control at atomic scale over both layer thickness and composition. ALD is based on a self-limiting and layer-by-layer approach that enables the deposition of a broad range of materials (oxides, nitrides, phosphates, sulfides, metals) on both inorganic and polymeric supports [23-25]. One of the main advantages of ALD is its ability to form homogenous monolayers over large surface areas and high aspect ratio nanoporous substrates. This novel strategy that combines nanoporous alumina platforms and ALD conformal deposition of thin film oxides, allows them to be employed in many applications as new and innovative biologically derived materials for medical device industry, such as bioelectronics, biosensors, drug delivery devices, tissue-engineering scaffolds and bioassay devices [26-28].

In the case of NPA-bSs application as membranes, permeability and permselectivity (or preferential permeation of a component in comparison with another one) are two key parameters related to membrane performance, but durability, involving both fouling prevention and long-term stability, is also another important factor. Consequently, antifouling and biocompatibility characteristics of membranes surfaces are also of significant importance. On the other hand, from an optical standpoint, NPASs are binary composite matrices formed by air and alumina, and the spatial distribution of these two components at the nanoscale establishes their macroscopic optical properties such as the effective refractive index and dielectric constant, which can be estimated by averaging the properties of both individual constituents [29-30]. In addition, since these engineered nanomaterials enable a precise control of light–matter interactions, they can be utilized as a platform to develop photonic crystal structures [31-32].

Moreover, the interesting optical properties exhibited by NPASs, such as its photoluminescence response in the UV-visible range, have been applied in many research areas, due to the specific interaction of light with a porous medium, by exploiting the different kinds of interactions that can take place between the incident light beam and several sections of the porous media (alumina surface layer, inner pore wall or the medium inside the pores), which are also strongly dependent on the characteristic geometrical parameters of the porous alumina membrane (e.g., pore diameter, interpore distance, wall thickness, oxide layer thickness), and its chemical composition that can also be modified after incorporation of organic or metallic pigments acting as a decorative layers [33].

Despite the numerous studies of NPASs for optical sensing and bio-sensing applications, the modification of their selectivity and optical properties induced by surface modification with functional oxide thin films has not been yet extensively reported. In this work, we analyze the morphological, chemical, electrochemical and optical characteristics of nanoporous alumina-based structures (NPA-bSs) obtained by deposition of different metal oxides (ZnO, TiO_2, Fe_2O_3 or Al_2O_3) by ALD technique on a ceramic NPAS synthesized by the two-step aluminum anodization method using a sulfuric acid solution as electrolyte (aspect ratio higher than 2000). Morphological and chemical surface changes of the NPA-bSs associated to the surface and pore-walls coverage by ALD technique were determined by scanning electron microscopy (SEM) and X-ray photoelectron spectroscopy (XPS), while depth-profile XPS analysis was performed to establish the nanopore-walls coating. The effect of metal oxides coverage on the electrochemical behavior (effective fixed charge and diffusion transport coefficient ratio) of the NPA-bSs was determined by concentration potential measurements, which were carried out with NaCl solutions at different concentrations, while optical characteristics of the analyzed samples were determined by transmittance measurements. This set of experiments provides wide information on NPA-bSs particular features and the obtained results would allow us to determine the most adequate surface modification of the NPA-bS for a specific application. In fact, coating materials were selected by considering their antifouling properties or slight electronegative character when compared with alumina, in order to enhance the transport properties when used as membranes, but also due to their differences in optical characteristic parameters (refraction index or band gap) as a way to broaden the application of NPA-bSs to optical devices.

2. Experimental

2.1. Synthesis of a nanoporous anodic alumina structure and metal oxides surface coating by Atomic Layer Deposition

The NPAS used as support in this study were synthesized by the electrochemical two-step anodization technique [11, 14] using an aqueous solution of sulfuric acid (0.3 M) as electrolyte solution. During the whole anodization process, vigorous stirring was employed to ensure the homogeneity of the bulk electrolyte concentration, while temperature was kept constant by using an external recirculating cooler. High purity aluminum discs (Al 99.999 %, Goodfellow, UK), 0.5 mm thick, were used as starting substrates for the fabrication of the NPAS. Prior to the first anodization, the Al foils were cleaned by sonication in isopropanol and ethanol, and subsequently electropolished in a 1:3 vol. solution of perchloric acid in ethanol under vigorous stirring at a voltage of 20 V. The duration of the first anodization step was set to 24 h, under an applied anodization voltage of 25 V at 0-1 ºC. After the first anodization step, the aluminum oxide layer grown was selectively removed by immersing the samples in an acidic solution of CrO_3 and H_3PO_4 at 35 ºC for 24 h. The second anodization step was performed under the same anodization conditions as the first one, but in this case the anodization time was adjusted until the NPAS achieves a thickness of ~ 60 μm. Afterwards, an aqueous mixture of HCl and $CuCl_2$ was employed to remove an area of around 1 cm^2 of the NPAS backside. The alumina barrier layer that blocks the pores bottom was removed by wet chemical etching in H_3PO_4 5% aqueous solution at room temperature during 40 min. Finally, the pores were widened by chemical etching in an aqueous solution of phosphoric acid (5 wt. %) during 4 min at 30°C.

ALD coating of the NPASs was performed in a Savannah 100 thermal ALD reactor from Cambridge Nanotech (Waltham, MA, USA), working in exposure mode, as schematically shown in Fig. 1 a. Different metal-organic compounds (trimethylaluminum, ferrocene, diethylzinc, titanium tetraisopropoxide), were used as precursors for the deposition of the different conformal coating layers (Al_2O_3, Fe_2O_3, ZnO and TiO_2), as explained in a previous work [21]. In all cases, high purity Ar was employed as carrier gas. Depending on the specific chemistry of the ALD precursor employed for NPASs functionalization, either H_2O (18.2 MΩcm) or O_3 supplied by an integrated ozone generator, were employed as oxidant agents, being also responsible for the substrate functionalization. During the ALD process, NPASs were exposed to the different precursors in sequential order (Fig. 1 a (i, iii)), with varying the exposure times in the range of 45-60 s to assure gaseous precursors diffusion through the pores of the NPASs. Specific precursors and temperatures are indicated in Table 1. An extended purge (90 s) with an Ar flow of 50 sccm, was performed between two subsequent precursor pulses, in order to remove the

excess of reactants and resulting by-products of the ALD process (Fig. 1 a (ii, iv)). The number of ALD cycles was selected in order to adjust the thickness of the deposited layer to around 5 nm in base to the different growth rates of each metal oxide [21, 24, 34]. Fig. 1b (i) shows the scheme of an ideal bare NPAS (aspect ratio higher than 2000), while the ideal nanoporous alumina-based structure after surface coating by a ceramic oxide layer by ALD is shown in Fig. 1b (ii).

Table 1: Precursors and deposition conditions employed for the ALD coating of different functional oxides on the surface and pores of the NPASs.

Oxide layer	ALD precursors	Precursor Temperature (ºC)	Substrate Temperature (ºC)
Al_2O_3	H_2O	60	200
	Trimethylaluminum ($C_6H_{18}Al_2$)	20	
Fe_2O_3	O_3	20	230
	Ferrocene ($C_{10}H_{10}Fe$)	100	
ZnO	H_2O	60	200
	Diethylzinc ($C_4H_{10}Zn$)	20	
TiO_2	H_2O	60	200
	Titanium tetraisopropoxide ($C_{12}H_{28}O_4Ti$)	75	

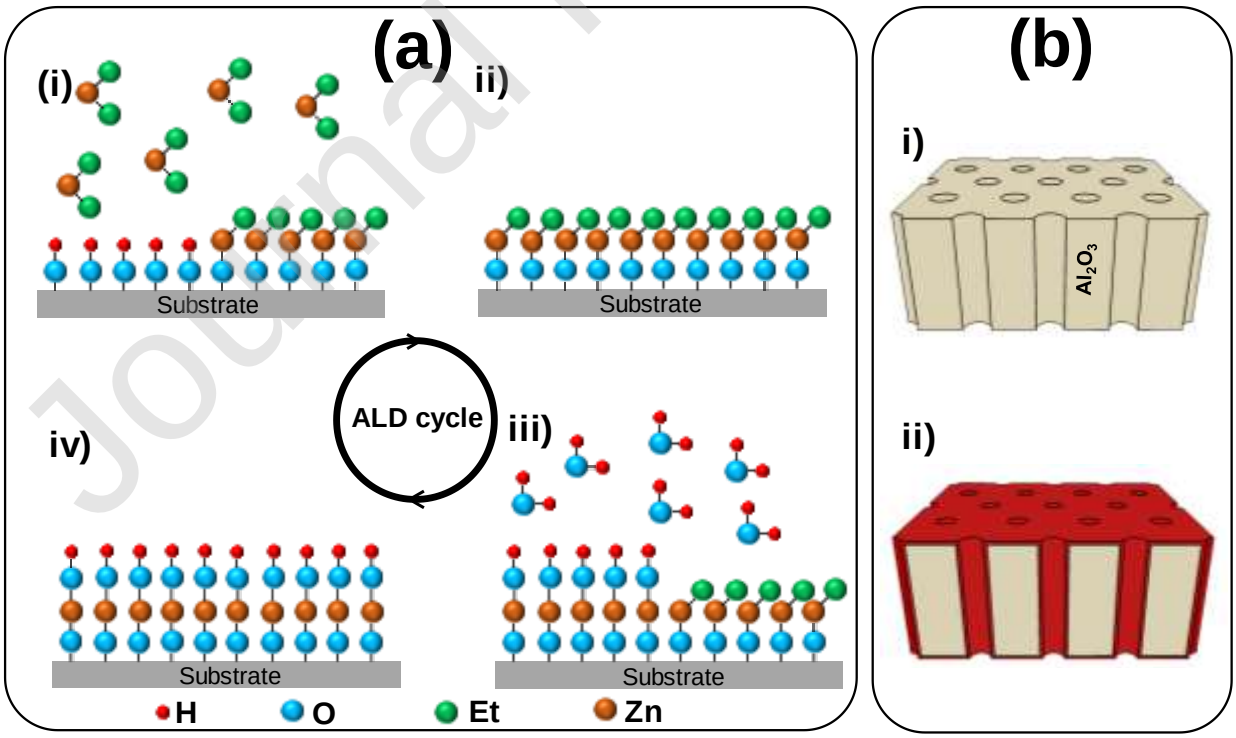

Fig. 1: (a) ALD deposition cycle of ZnO: (i) and (iii) exposure to precursors, DEZ and H_2O, respectively; (ii) and (iv) Purge of the excess of precursor and reaction subproducts after surface saturation. (b) Scheme of an ideal: (i) nanoporous alumina structure (NPAS) obtained by the two-step anodization method with pore length of around 60 μm; (ii) NPA-bS after surfaces coating by ALD technique.

2.2. Chemical surface analysis

XPS is a non-destructive surface sensitive technique commonly used to determine or confirm the empirical formula of a material and the quantity of the elements present in the surface or near the surface (around 2-8 nm depth) [35]. Chemical surface characterization of the ALD coated NPA-bSs was performed by analyzing XPS spectra obtained with a Physical Electronics Spectrometer (PHI 5700) with X-ray Mg K_α radiation (15 kV, 300W and 1253.6 eV) as the excitation source. A concentric hemispherical analyzer, operating in the constant pass energy mode at 29.35 eV, was used for recording the high-resolution spectra at a take-off angle of 45º. The diameter of the analyzed area was 720 μm and each spectral region was scanned several times in order to have a good signal (low noise contribution). The residual pressure in the analysis chamber was maintained below 5×10^{-7} Pa during data acquisition, and binding energies (accurate ±0.1 eV) were determined with respect to the position of the adventitious C 1s peak at 285.0 eV. PHI ACCESS ESCA-V8.0 F software package was used for data acquisition and analysis [36].

Depth-profile XPS analysis, a sample-destructive testing process, was also performed by argon sputtering (4 kV and 1.5 mA) during 8 min. This technique allows us an estimation of surface environmental contamination as well as layers characteristic and thickness [37].

2.3 Scanning electron microscopy characterizations

Surface morphological parameters of NPA-bSs were studied by SEM analysis. Measurements were performed in a JEOL JSM-5600 microscope operated at 20 kV, which is also equipped with an Oxford INCA energy dispersive X-ray spectroscopy (EDS) microanalysis system. SEM images were obtained after samples coating with a thin Au metallic layer by magnetron sputtering deposition (Polaron SC7620) during 180 s at 20 mA, to ensure their electrical conductivity, and they were further analyzed by using ImageJ software [38].

2.4. Optical characterization by transmittance and spectroscopic ellipsometry measurements

Transmittance spectra were recorded with a Varian Cary 5000 spectrophotometer (Agilent Technologies, USA) provided with an integrating sphere of Spectralon for a wavelength interval of 200-2000 nm.

Spectroscopic Ellipsometry (SE) measurements were carried out with a spectroscopic ellipsometer (Sopra-Semilab GES-5E) using wavelengths in the range from 400 nm to 1600 nm at an incident angle of 70°. SE measurements were performed with unsupported samples. WinElli software from Sopra-Semilab was used for data analysis and fittings.

2.5. Membrane potential measurements

Membrane potential ($\Delta\Phi_{mbr}$), or the equilibrium electrical potential difference between two electrolyte solutions of different concentration (C_f and C_V) separated by a membrane was determined from concentration potential (ΔE) measured in the test-cell showed in Supplementary Information (Fig. S1) following the experimental procedure indicated in previous papers [21, 39], using NaCl solutions (C_f = 0.01 M, while C_V ranged between 0.002 M and 0.1 M) and Ag/AgCl reversible electrodes connected to a digital voltmeter (Yokohama 7552, 1GΩ input resistance). $\Delta\Phi_{mbr}$ values were obtained by subtraction of electrode potential ($\Delta\Phi_{elc} = (RT/F)\cdot\ln[C_V/C_f]$) to measured ΔE values. Measurements were carried out at room temperature (25 ± 2) ºC and standard pH (5.8 ± 0.3), with solutions stirred at 540 rpm to minimize interfacial effects [39].

3. Results and discussion

3.1. Morphological and chemical characterizations of the nanoporous alumina-based structures

Top view SEM images of the NPAS, as well as of ALD coated NPA-bSs have been analysed in order to verify the uniform hexagonal pore distribution and to determine the values of average pore radius ($<r_p>$) and its further reduction due to the ALD-coating layer. Fig. 2.a displays a micrograph of an as-produced NPAS, whereas the image in Fig. 2.b corresponds to the NPAS+ZnO sample, both images being taken at the same magnification value. All samples present the same interpore distance, D_{int} = 65 nm, but variation in pore size associated to the ALD coating, which becomes evident by direct comparison between both images in Fig. 2.a and 2.b. The initial value of $<r_p>$ has been determined to be 14 ± 2 nm employing computer assisted image analysis techniques [40]. The average pore radius is reduced to 9 ± 2 nm after ALD deposition of ZnO, and takes similar values for the other studied oxides, as shown in Table 2. These values

obtained from SEM analyses are in good agreement with the estimated deposited thickness of 5 nm for the different oxides. From the measured values of the pore diameter, the porosity of the samples was calculated basing on the symmetry of highly ordered hexagonal pore distribution ($\Theta = (2\pi/\sqrt{3})\times(r_p/D_{int})^2$, [11]). The uniformity of the pores throughout the membranes was assessed through SEM cross section images, in which the straight and narrow pore channels are clearly visible (inset in Fig. 2.a).

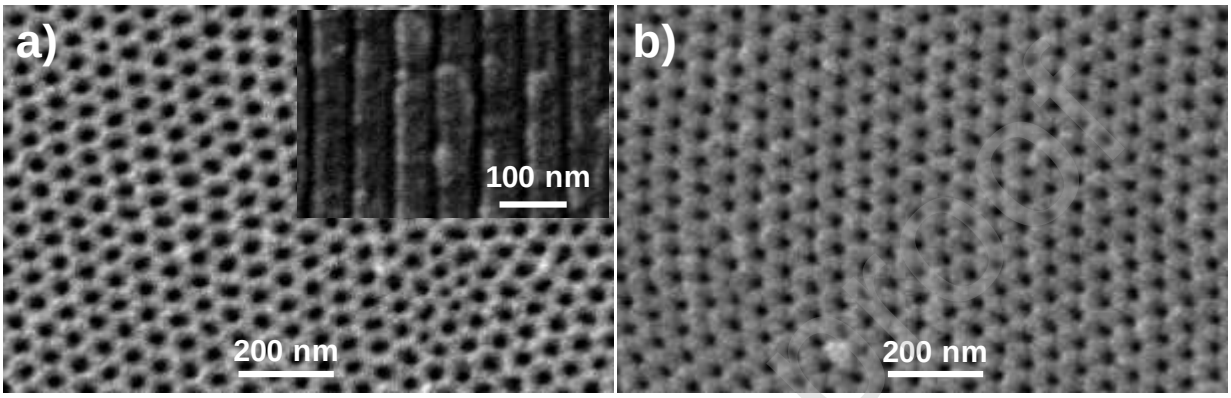

Fig. 2: SEM micrographs of the surface of NPAS (a) and NPAS+ZnO (b) samples. The inset in a) sows a cross section view of the parallel aligned channels of the NPAS sample.

Table 2: Average values of surface pore radius ($<r_p>$) and porosity ($<\Theta>$) for the studied NPA-bSs.

Membrane	$<r_p>$ (nm)	$<\Theta>$ (%)
NPAS+Al_2O_3	9 ± 2	7 ± 2
NPAS+TiO_2	10 ± 2	9 ± 2
NPAS+Fe_2O_3	9 ± 2	7 ± 2
NPAS+ZnO	9 ± 2	7 ± 2

Surface chemical characterization of the nanoporous structures was performed by analyzing the XPS spectra, that is, the curve of the core level photoemissions of the elements present on the samples surfaces, and the atomic concentration percentage (A.C. %) of each element is determined by the curve area. As an example, Fig. 3 shows a comparison of the oxygen spectra, the common characteristic element for all the NPA-bSs, where differences in the binding energy

(B.E.) of the corresponding peaks can be observed, which is an indication of different surface materials. The NPAS+Al_2O_3 sample shows a peak at the B.E. of 532.0 eV, which corresponds to alumina (B.E. between 531.6 and 532.4 eV [41]), while the spectra for the NPAS+TiO_2 sample shows a rather well-defined peak at a B.E. of 530.0 eV, associated to the TiO_2 coverage [33], which represents the 90 % of the total curve area, and a small alumina contribution at 532.0 eV (10 % of the total area). The oxygen spectra for the NPAS+Fe_2O_3 sample also exhibits a peak at around 530.0 eV (71 % of total curve area), associated to the Fe_2O_3 layer (B. E. at 529.6 eV for pure element [41]) and a shoulder at 532.0 eV (29 % of curve area), indicating the detection of the alumina substrate, while in the case of the NPAS+ZnO sample a wide peak was obtained, which might be deconvoluted in two different peaks, one at around 530.9 eV associated to ZnO [41-42] (49.7 % of total curve area) and the other at 532.2 eV (50.3 % of total area) attributed to the contribution of the alumina substrate.

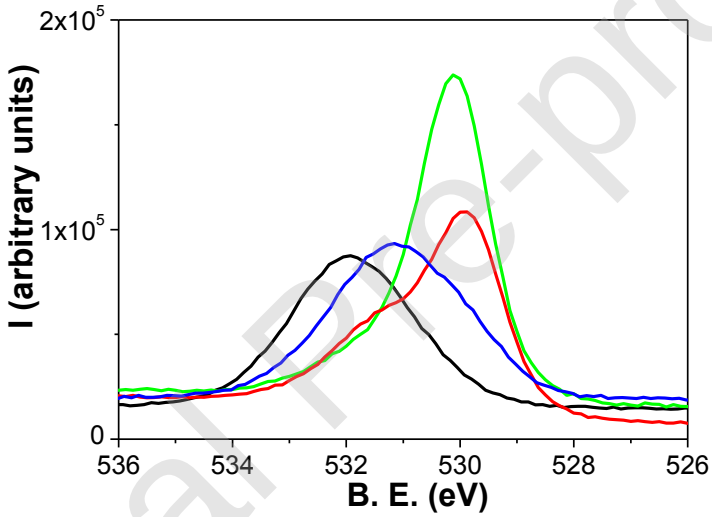

Fig. 3: Oxygen core level spectra for the analyzed samples: NPAS+Al_2O_3 (black line), NPAS+TiO_2 (green line), NPAS+Fe_2O_3 (red line) and NPAS+ZnO (blue line).

The atomic concentration percentages (A.C. %) of the different elements found on the external surface of the NPA-bSs analyzed are indicated in Table 3. As it can be observed, the surfaces of all the samples exhibit high percentage of carbon, which could be due to manufacture contamination associated to the precursors used for ALD coverage (see formulae in Table 1), although environmental contamination might also exist [43-45]. Moreover, values in Table 3 also show a practically total coverage of the alumina nanoporous support in the case of NPAS+TiO_2 and NPAS+Fe_2O_3 samples, while it seems to be partial in the case of the NPAS+ZnO sample according to the aluminum A.C. % determined, attributed to the patterned alumina support.

Table 3: Atomic concentration percentages of the elements found on both surfaces of the studied samples*

Sample	C (%)	Al (%)	O (%)	Ti (%)	Fe (%)	Zn (%)	N (%)
NPAS+Al_2O_3	43.6	15.7	37.7	---	---	---	2.0
NPAS+TiO_2	19.2	0.6	55.5	23.5	---	---	0.7
NPAS+Fe_2O_3	25.9	2.1	54.6	---	16.3	---	0.5
NPAS+ZnO	43.3	8.7	37.6	---	---	10.2	0.4

* other elements with A.C. % ≤ 0.5 are not indicated.

To verify the presence of the metal oxide layer along the pore-wall length as well as the superficial character of environmental contamination, XPS depth-profile analysis was also performed. Fig. 4.a shows the variation with the Ar sputtering time of the atomic concentrations of the characteristic elements for the NPAS+Fe_2O_3 sample, while a scheme of Ar sputtering effect on the analyzed sample is shown in Fig. 4.b. The first main effect of Ar sputtering (i) seems to be the elimination of the contamination layer (associated mainly to aliphatic carbon [43]) on the external surface of the sample, which reduces significantly the A.C. % of carbon (~ 85 %) after 0.5 min of argon sputtering and increases correspondingly the A.C. % values of the other characteristic elements (30 % for Fe, 400 % for Al and 3 % for O), leaving the Fe_2O_3 cover layer as external surface of the sample. The subsequent effect of Ar sputtering is the elimination of that external Fe_2O_3 layer (ii), which causes a decrease in the Fe % , until a constant value of around 7.5 % was reached, and a significant increase in the Al % (~ 50 %); finally, the analyzed surface corresponds to the bulk sample structure, that is, the alumina support and the Fe_2O_3 layer on the pore-walls (iii), and constant values for the atomic concentration percentages of the analyzed elements were obtained. These results are in good agreement with EDS composition profile obtained in a cross section of the NPAS+Fe_2O_3 sample shown in the supplementary information (Figure SI2), which confirms the presence of an approximately constant iron signal along the pore channels, whereas more intense peaks of both, iron and carbon are obtained near the external surfaces of the sample. Moreover, a comparison of the oxygen spectra for the NPAS+Fe_2O_3 sample obtained at two different sputtering times (t = 0 and t = 5 min) is shown in Fig. 4.c, where the elimination of the Fe_2O_3 peak at 530.0 eV obtained at the sample surface after 5 min of Ar sputtering is clearly observed. Angle-resolved XPS results allow us to estimate a

thickness of around 5-7 nm for the Fe_2O_3 cover layer. A comparison of XPS depth-profile results for NPAS+ Fe_2O_3 and NPAS+ TiO_2 samples is presented as Supplementary Information (Fig. SI3).

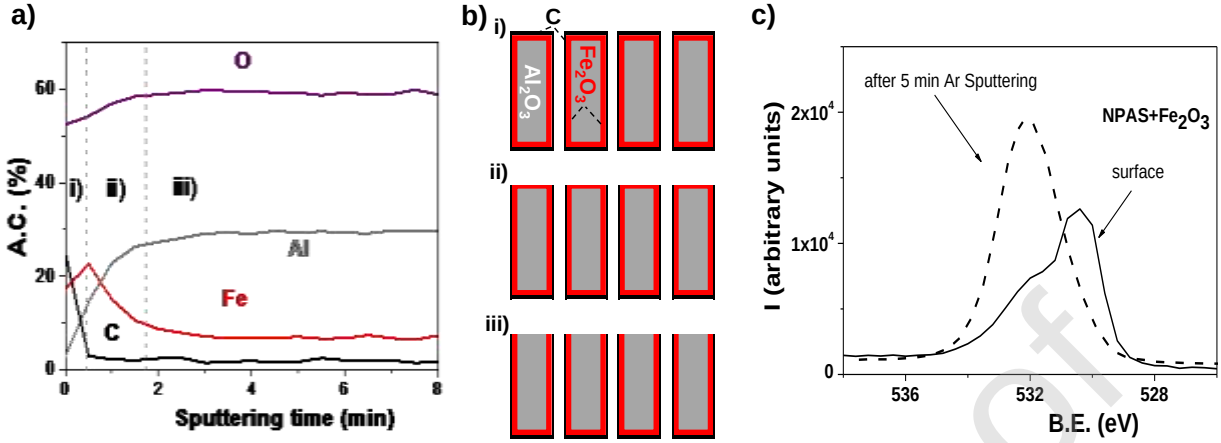

Fig. 4: (a) Atomic concentration % versus Ar sputtering time dependence for iron, aluminum, oxygen and carbon (profile curves) for the NPAS+Fe_2O_3 sample; (b) Schematics of Ar sputtering effect during XPS depth-profile analysis (c) Oxygen core level spectra for the NPAS+Fe_2O_3 sample at two different Ar sputtering times: dense line at t = 0 and dashed line at t = 5 min.

3.2. Optical characterization of NPA-bSs

The structure and surface materials of the NPA-bSs can play a key role in their optical properties, resulting in the generation of different optically active nanostructures. Both transmission and reflection techniques provide non-destructive methods for thin layer thickness determination as well as for the optical characterization of thin films or layers deposited on a solid matrix [46-51].

Fig. 5.a shows the variation of transmittance percentage with the light wavelength obtained for the metal oxides coated NPA-bSs, for UV-VIS wavelength region (200-2000 nm). According to these results, all the samples exhibit high transparency, with a maximum value of 91.0 % for the NPAS+Al_2O_3 sample, which is slightly reduced to around 88 % for all the metal oxide coated nanoporous structures in the near-infrared region, however, clear differences can be observed in the visible region. Due to the similarity in pore size/porosity of the studied samples, those changes seem to be related to the cover layer material. In fact, the small effect of geometrical parameters on transmittance curve can be observed in Fig. 5.b, where a comparison for three NPASs with different pore radii/porosity is presented.

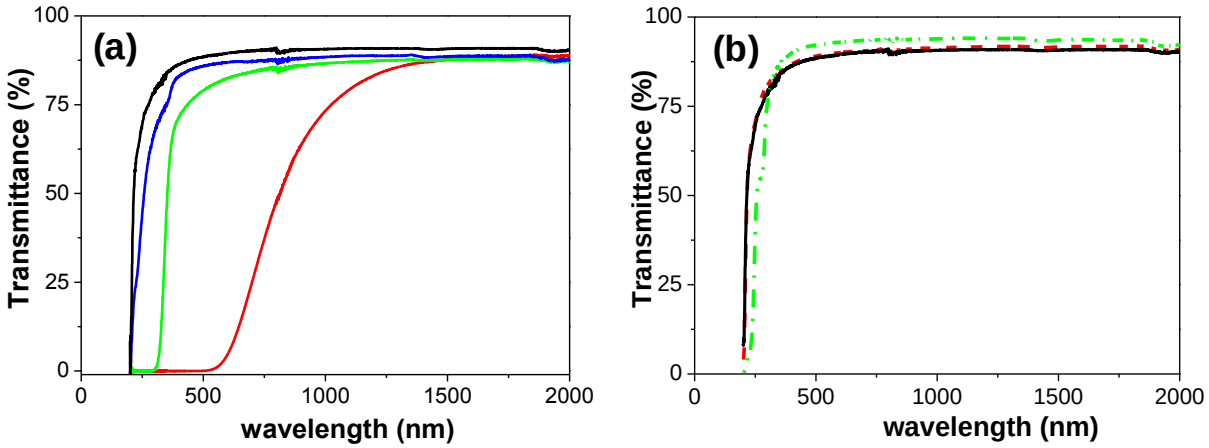

Fig. 5: (a) Transmittance versus wavelength for samples: NPAS+Al_2O_3 (black line), NPAS+TiO_2 (green line), NPAS+Fe_2O_3 (red line) and NPAS+ZnO (blue line). (b) Comparison of transmittance curves for three NPASs with different pore radii/porosity: 9 mn/7 % (black solid line), 12 nm/12 % (red dashed line), 23 nm/17 % (green dashed-dotted line).

Differences in another optical characteristic of great interest as it is the band gap of the studied samples were also obtained, and the values determined for each NPA-bS are indicated in Table 4 (both in eV and nm). When these values are compared with the theoretical ones of pure oxides cover-layers, rather good concordance in the case of NPAS+Fe_2O_3 and NPAS+TiO_2 samples can be observed (2.2 eV for Fe_2O_3 and 3.2 eV for TiO_2 (anatase) [52-53]) in agreement with the higher purity of both surface layers, while the value obtained for the NPAS+Al_2O_3 sample is coincident with that reported in the literature for amorphous films obtained by ALD technique (6.2 eV [54]). In the case of the NPAS+ZnO sample, the value of band gap differs significantly from the pure ZnO (3.3 eV for ZnO single crystals at room temperature [55]), but it could be associated to the relatively high percentage of aluminum on the surface of this sample, according to the values previously determined by XPS analysis (~ 9 % Al and ~10 % of Zn), and taking into account its effect in the band gap increases determined for Al doped ZnO samples indicated in the literature (increase from 3.4 eV to 3.90 eV with increasing the Al content from 0 to 2.4 % [56]).

Consequently, differences in band-gaps indicate diverse optical windows depending on the cover layer material (but practically independent of pore size/porosity), opening the possibility of easy optical tuning of the alumina-based nanoporous support [57].

Table 4: Band gap values determined for the different NPA-bSs.

Sample	Band gap (eV)	Band gap (nm)
NPAS+Al_2O_3	6.31	196.5
NPAS+TiO_2	3.91	317.5
NPAS+Fe_2O_3	2.12	585.1
NPAS+ZnO	6.41	193.4

Information on optical changes associated to both film surface and bulk phase modifications can also be obtained from SE measurements. In particular, SE allows for the determination of the ellipsometric angles, Ψand Δ, two experimental parameters related with the amount of reflected light polarized in the perpendicular plane with respect to the incidence light plane (r_p) and the amount of reflected light polarized in a plane parallel to the incidence light plane (r_s), through the following expression [47]: $\tan(\Psi) \times e^{i\Delta} = r_p/r_s$, where tan(Ψ) is the amplitude ratio upon reflection and Δis the phase shift difference. Since SE measurements have been performed for wavelength ranging between 400 nm and 1600 nm, optical information on visible and near infrared regions may be obtained.

Fig. 6 shows the variation with the wavelength of both SE experimental parameters (tan(Ψ) in Fig. 6.a and cos(Δ) in Fig. 6.b), and differences in the curves depending on the ceramic oxide cover-layer can be observed, being those differences more significant for cos(Δ), and they could be related to material/structural characteristic of a particular cover-layer (layer thickness and crystalinity, pore radii/porosity, surface smoothness, nanoparticles size or material defects/impurities, ..) [49-52], while silgth interference fringes at high wavelength values might be related to samples transparency [58].

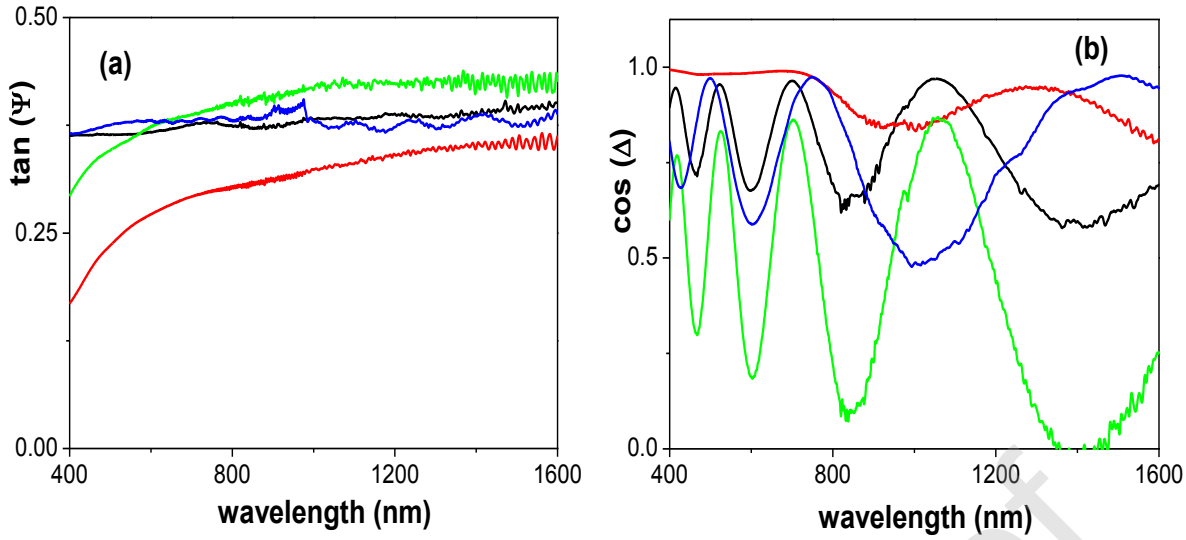

Fig. 6: Light wavelength dependence of: (a) tan(Ψ), and (b) cos(Δ), for NPAS+Al_2O_3 (black line), NPAS+TiO_2 (green line), NPAS+Fe_2O_3 (red line) and NPAS+ZnO (blue line) samples.

Optical characteristic parameters such as the refractive index (n) and the extinction coefficient (k) were determined from SE measurements using the ellipsometer software, and their dependence on wavelength is shown in Fig. 7.a and 7.b. Moreover, SE results also provide information on the dielectric constant taking into account that $\varepsilon = (n + i \cdot k)^2$ [47], and its change with the wavelength for the different samples is shown in Fig. 7.c. Differences in curve shape for these three optical parameters depending on coating layer material were obtained, although values are rather similar in the case of NPAS+Al_2O_3 and NPAS+ZnO samples, mainly in the visible region; this fact could be related with the partial coverage by the ZnO layer of the alumina support, as it was already determined by XPS results, or the similarity of optical parameters of both materials, in agreement with band-gap values.

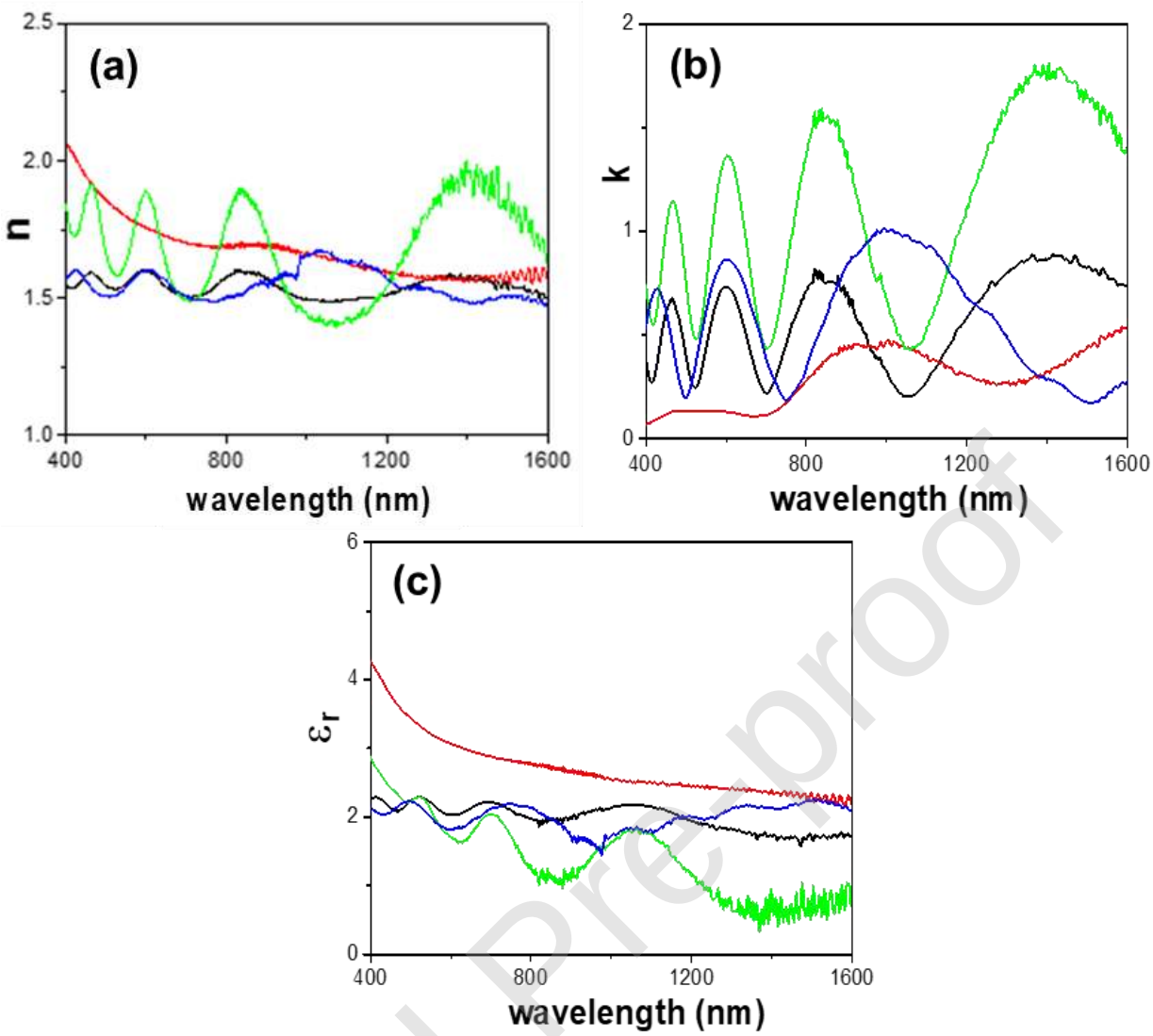

Fig. 7: Wavelength dependence of: (a) refraction index, (b) extinction coefficient, and (c) dielectric constant for NPAS+Al_2O_3 (black line), NPAS+TiO_2 (green line), NPAS+Fe_2O_3 (red line) and NPAS+ZnO (blue line) samples.

The effect of sample geometry in SE values can be observed in Supplementary Information (Fig. SI4), where a comparison of the refraction index and the extinction coefficient determined for three alumina anodized structures with different pore size/porosity: NPAS (r_p = 12 nm, Θ = 12%: solid line) NPAS* (r_p =23 nm, Θ = 17%: dashed line) and NPAS** (r_p = 110 nm, Θ = 20%: dashed-dotted line) is presented. According to these results, the oscillatory dependence with wavelength of both optical parameters (n and k) seems to be related with pore size, and a clear reduction in the oscillatory behavior with pore increase can be observed. Moreover, layer structure can also affect SE results, and Fig. SI5 in Supplementary Information shows the

variation of the ellipsometric parameter Ψ with the light-incident angle (60º, 65º, 70º and 75º) for the NPAS+Fe_2O_3 sample. Due to the fact that lower light-incident angle (60º) allows deeper sample analysis than that associated to high angle (75º), curves differences are attributed to superficial sample impurities/inhomogeneity. Moreover, since the curves obtained are rather similar in the visible region to that reported in the literature for a Fe_2O_3 layer deposited on highly oriented pyrolytic graphite support [59], this concordance validates the reliability of the determined values.

For comparison reason, average values for the refractive index, extinction coefficient and dielectric constant for visible (v) and near infrared (nir) regions were independently determined and they are indicated in Table 5. According to literature values for the pure ceramic oxides forming the cover layer of the analyzed samples (n(Fe_2O_3) = 2.7, n(TiO_2) = 2.5, n(ZnO) = 2.4 and n(Al_2O_3) = 1.76 at λ = 589 nm)) [60], the tendency of the refractive index for the studied samples in the visible region seems to be similar to that of the pure ceramic oxides (taking into account the presence of aluminum in the surface of the NPAS+ZnO sample already commented analyzing XPS results). In any case, it should be considered that the value of the refraction index obtained from SE measurements for porous samples corresponds to an "effective" refraction index, which includes the contribution of both the solid structure and the air in the pores [29-30]. Consequently, a slight reduction in the refractive index of the four studied samples was expected, being 12 % in the case of the NPAS+Al_2O_3 sample, but higher reduction (~ 30 %) for the other NPA-bSs, which could be an indication of alumina support contribution. In fact, average refraction index value for the NPAS+Al_2O_3 sample are in agreement with values already reported for similar aluminium anodic nanoporous samples ($1.52 \leq n \leq 1.62$; samples with 15 nm pore radii, 9 % porosity and thickness ranging between 9 μm and 45 μm [61]).

Table 5. Average values of refractive index, extinction coefficient and dielectric constant <ε> for the studied NPA-bSs for the visible region (v) and near infrared region (nir).

sample	$<n_{vr}>$	$<k_{vr}>$	$<\varepsilon_r^{vr}>$ (F/m)	$<n_{nir}>$	$<k_{nir}>$	$<\varepsilon_r^{nir}>$ (F/m)
NPAS+Al_2O_3	1.55 ± 0.03	0.48 ± 0.16	2.15 ± 0.09	1.54 ± 0.03	0.64 ± 0.22	1.91 ± 0.17
NPAS+TiO_2	1.69 ± 0.14	0.87 ± 0.29	2.05 ± 0.43	1.69 ± 0.19	1.27 ± 0.44	1.09 ± 0.41
NPAS+Fe_2O_3	1.81 ± 0.12	0.13 ± 0.04	3.26 ± 0.46	1.62 ± 0.05	0.38 ± 0.08	2.47 ±0.14
NPAS+ZnO	1.54 ± 0.04	0.51 ± 0.22	2.06 ± 0.13	1.55 ±0.06	0.59 ± 0.29	1.98 ± 0.19

According to these results, optical characterizations performed with the functional NPA-bSs here studied show differences in characteristic parameters, depending on the ceramic oxide used as the coating layer, which opens their possible use in specific applications of optical devices, such as in photoluminescent and interferometric biosensors for enzymatic biosensing, light waveguides sensors and optical filters, and other photonic platforms [62-64].

3.3. Electrochemical characterization of NPA-bSs by membrane potential measurements

Among the most common applications of nanoporous structures with narrow pore-size distribution are membranes for diffusive solute transport [65-68]. A membrane can be defined as a physical barrier allowing selective transport of mass species and, consequently, low nanoparticle/pore-size ratio is a requirement for transport control, but sample hydrophobicity, porosity and membrane fixed charge are also significant characteristics when transport of aqueous solutions and charged particles or ions are involved [69].

In such applications, the analysis of diffusive ions transport is usually considered by determining the ionic transport numbers (t_i), which represent the fraction of the total current transported for each ion ($t_i = I_i/I_T$), the ionic diffusion coefficients ($D_i = |z_i|t_i/[|z_+|t_+ + |z_-|t_-]$, being z_i the ion valence) and the effective fixed charge concentration (X_{ef}), which might affect rejecting/favoring the transport of co-ions/counter-ions (ions of similar/opposite sign that the membrane charges) across the membrane [70]. Moreover, the effective fixed charge concentration in a membrane also affects the interfacial or Donnan equilibrium, that is, the distribution of ions in the liquid part of the solution/membrane interface [71]. According to the Teorell-Meyer-Sievers (TMS) model [72-73], the equilibrium electrical potential difference between two electrolyte solutions of concentrations (C_f and C_v) separated by a membrane is given by the contribution of two Donan potentials (one for each solution/membrane interface) plus a diffusion potential of the ions inside the membrane, and it can be expressed by [71]:

$$\Delta\Phi_{mbr} = -\frac{RT}{wzF}\left[U \ln\frac{\sqrt{4y_v^2+1}+wU}{\sqrt{4y_f^2+1}+wU} - \ln\frac{c_f}{c_v}\frac{\sqrt{4y_v^2+1}+w}{\sqrt{4y_f^2+1}+w}\right] \quad (1)$$

being F and R the Faraday and gas constants, while T represents the temperature of the system and w = (+1)/(-1) depending on the electrical character of the membrane (positive/negative fixed charge). The parameters U and y_i are related to the ions transport numbers, the effective fixed charge concentration and the electrolyte concentration in the membrane [21, 39].

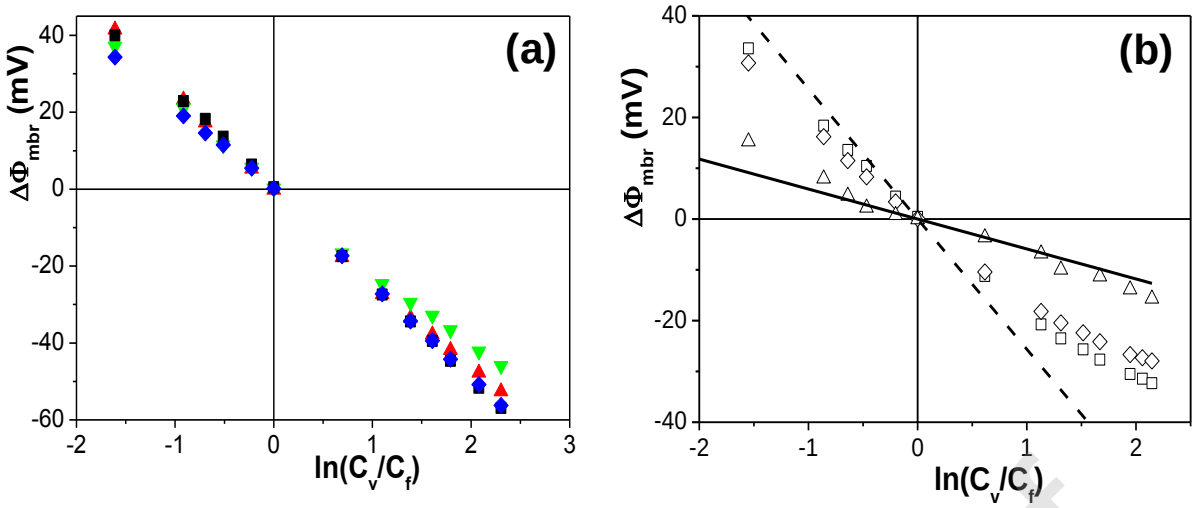

Fig. 8: Membrane potential as a function of the solutions concentration ratio for: (a) NPAS+Al_2O_3 (■), NPAS+Fe_2O_3 (▲), NPAS+TiO_2 (▼) and NPAS+ZnO (♦) samples. (b) NPAS (r_p = 12 nm, Θ = 12 %) (□), NPAS* (r_p =23 nm, Θ = 15 %) (◊) and NPAS** (r_p = 110 nm, Θ = 20 %) (Δ).

Dependence of membrane potential with the solution concentrations ratio (C_v/C_f) for the studied samples is shown in Fig. 8.a, where only slight differences depending on the material of the cover layer can be observed, which could be an indication of pore-size control of diffusive transport. This point can be more clearly observed in Fig. 8.b where a comparison of membrane potentials for three alumina nanoporous membranes or structures (with different pore size/porosity (NPAS: 12 nm/12 %, NPAS*: 23 nm/17 % and NPAS**: 110 nm/20 %) are presented; moreover, membrane potentials for an ideal positively charged membrane (a membrane with $t_- = 1$ and $t_+ = 0$) and the solution diffusion potential (that is, without membrane contribution) are also indicated in Fig. 8.b by dense and dotted lines, respectively. Results in Fig. 8.b clearly show the reduction of barrier effect with the increase of sample pore size and porosity. This behavior seems to be independent of surface material according to the results shown in Fig. SI6 in Supplementary Information for two NPAS+TiO_2 samples with different geometrical parameters.

The fitting to Eq. (1) of the values shown in Fig. 8.a, following the calculation procedure indicated in previous papers [21, 74], allows for the determination of the effective fixed charge and ion transport numbers across the NPA-bSs as well as the ionic diffusion coefficients ratio ($D_-/D_+ = t_-/t_+$). The values of X_{ef} , t_+ and D_-/D_+ obtained for each sample are indicated in Table 6. A comparison of the ionic diffusion coefficients ratio in the NPA-bSs with that corresponding to

the ions in solution, $(D_{Cl^-}/D_{Na^+})^o = 1.20$ [75], reveals the significant influence of the coating layer on the diffusive transport of ions through the nanopores, favoring the counter-ion (anion) transport with respect to the co-ion (cation) one. This effect is easily quantified by considering the "membrane permselectivty" (PS) or charge selectivity, which can be calculated from the transport number of the counter-ions and co-ions in the membrane and the outside solutions; taking into account the electropositive character of all the samples [70]:

$$PS = (t_{counter} - t^o_{counter})/t^o_{co} \quad (2)$$

where $t_{counter}$ corresponds to the transport number of the counter-ion (Cl-) through the pores of the membrane, $t^o_{counter}$ is the transport number of the counter-ion in solution and t^o_{co} the transport number of the co-ion in solution. PS values for the different NPA-bSs are also indicated in Table 6. Taking into account the similarity in pore radii and porosity of the analyzed samples, these results show basically the effect of the coating material on the diffusive transport of ionic solutions across the different NPA-bSs as a result of different effective fixed charge and hydrophobic/hydrophilic character of the cover layer. These results are consistent with those previously obtained [21] for NPA-bSs with similar coverage but higher pore size (~ 25 % higher), which present lower values of fixed charge and permselectivity but similar tendency with respect to the effect of material surface (see Table SI1 in Supplementary Information).

Table 6: Effective fixed charge (X_{ef}), cation transport number (t_+), anionic permselectivity (P_-) and ionic diffusion coefficients ratio (D_{Cl^-}/D_{Na^+}) for the studied NPA-bSs.

Sample	X_{ef} (M)	t_+	D_{Cl^-}/D_{Na^+}	P (%)
NPAS+Al_2O_3	+ 0.026	0.129	6.7	66.5
NPAS+TiO_2	+ 0.015	0.268	2.7	30.4
NPAS+Fe_2O_3	+ 0.019	0.198	4.0	48.6
NPSAS+ZnO	+ 0.025	0.115	7.7	70.1

Conclusions

Geometrical parameters and surface material features of a nanoporous alumina structure, NPAS, or membrane, with 12 ± 2 nm pore radii and 12-15 % average porosity have been successfully modified by covering their surfaces with layers of different metal oxides (TiO_2, Fe_2O_3, ZnO and Al_2O_3) by ALD technique, in order to get new nanoporous alumina-based structures, NPA-bSs, with modified characteristics. Analysis of SEM images and XPS depth-profile spectra has permitted us to determine rather similar geometrical parameters for all the NPA-bSs, with a reduction of around 30 % in pore size and 50 % in porosity with respect to the original patterned support, and a cover-layer thickness of ~ 5-7 nm for the studied samples.

Moreover, coverage material also affects the values of optical characteristic parameters of the NPA-bSs, especially the band-gap values, but also the refractive index, extinction coefficient and dielectric constant, mainly when specific wavelength for the visible and near-infrared regions are compared, being more significant in the case of Fe_2O_3 coverage. On the other hand, differences in diffusive electrolyte transport characteristic parameters such as effective fixed charge, ion transport numbers or ionic permselectivity depending on the nature of the coating layer were also determined, with the following sequence for permselectivity values: NPAS+ZnO ≈ NPAS+Al_2O_3 > NPAS+Fe_2O_3 >> NPAS+TiO_2.

Consequently, ALD technique seems to be an adequate method for geometrical and functional changes of alumina-based nanoporous structures, opening their most common field of application as nanofilters or membranes for drug delivery systems, to more specific performance or platforms for biosensors or optical sensing devices.

Declaration of interests

The authors declare that they have no known competing financial interests or personal relationships that could have appeared to influence the work reported in this paper.

Acknowledgement

This work has been financial supported partially under MINECO Research Project No. MAT2016-76824-C3-3-R and FISS-19-DTS19/00088. The scientific support from the SCT's of the University of Oviedo (Nanoporous Membranes Laboratory and Electronic Microscopy units) and the SCBI (Supercomputer and Bioinformatics Service) of Málaga University are also acknowledged.

References

1. Losic, D.; Simovic, S. Self-ordered nanopore and nanotube platforms for drug delivery applications. *Exp. Opin. Drug Deliv.* **2009**, 6, 1363–1381.

2. Osmanbeyoglu, H.U.; Hur, T.B.; Kim, H.K. Thin alumina nanoporous membranes for similar size biomolecule separation. *J. Membr. Sci.* **2009**, 343, 1–6.

3. Logar, N. Z.; Tušar, N. N.; Ristić, A.; Mali, G.; Mazaj, M.; Kaučič, V. Functionalisation and Structure Characterisation of Porous Silicates and Aluminophosphates, in "Ordered Porous Solids", V. Valtchev, S. Mintova, M. Tsapatsis (eds.), Elsevier Science (**2009**), Chap. 5, pp. 101-126.

4. Gultepe, E.: Nagesha, D.; Sridhar, S.; Amiji, M. Nanoporous inorganic membranes or coatings for sustained drug delivery in implantable devices. *Adv. Drug Deliver. Rev.* **2010**, 62, 305–315.

5. McInnes, S.J.; Irani, Y.; Williams, K.A.; Voelcker, N.H. Controlled drug delivery from composites of nanostructured porous silicon and poly (l-lactide). *Nanomedicine* **2012**, 7, 995–1016.

6. Petukhov, D.I.; Napolskii, K.S.; Eliseev, A.A. Permeability of anodic alumina membranes with branched channels, *Nanotechnology* **2012**, 23, 335601.

7. Pavlikov, A.V.; Lartsev, A.V.; Gayduchenko, I.A.; Timoshenko, V.Y. Optical properties of materials based on oxidized porous silicon and their applications for UV protection. *Microelectron. Eng.* **2012**, 90, 96–98.

8. Vázquez, M. I.; Romero, V.; Vega, V.; García, J.; Prida, V. M.; Hernando, B.; Benavente, J. Morphological, chemical surface, and diffusive transport characterizations of a nanoporous alumina membrane. *Nanomaterials* **2015**, 5, 2192-220.

9. Porta-i-Batalla, M.; Xifré-Pérez, E.; Eckstein, C.; Ferré-Borrull, J.; Marsal. L. F. 3D Nanoporous Anodic Alumina Structures for Sustained Drug Release. *Nanomaterials* **2017**, 7, 227-239.

10. Medina-Llamas, M.; Mattia, D. Production of Nanoemulsions Using Anodic Alumina Membranes in a Stirred-Cell Setup. *Ind. Eng. Chem. Res.* **2017**, 56, 7541-7550.

11. Masuda, H.; Fukuda, K. Ordered metal nanohole arrays made by a two-step replication of honeycomb structures of anodic alumina. *Science* **1995**, 268, 1466-1468.

12. Martín, R.; Manzano, C.V.; Martín-González, M. In-depth study of self-ordered porous alumina in the 140–400 nm pore diameter range. *Micropor. Mesopor. Mat.* **2012**, 151, 311-316.

13. Santos, A.; Kumeria, T.; Losic, D. Nanoporous anodic aluminum oxide for chemical sensing and biosensors. *Trends Anal. Chem.* **2013**, 44, 25–38.

14. Lee, W.; Park, S-J. Porous anodic aluminum oxide: anodization and template synthesis of functional nanostructures. *Chem. Rev.* **2014**, 114, 7487-7556.

15. Bryant, W. A. The fundamentals of chemical vapour deposition, *J. Materials Sci.* **1977**, 12, 1285-1306.

16. George, S. M. Atomic layer deposition: an overview, *Chem. Rev.* **2010**, 110, 111–131.

17. Hierrezuelo, J.; Romero, V.; Benavente, J.; Rico, R.; López-Romero, J.M. Membrane surface functionalization via theophylline derivative coating and streptavidin immobilization; Colloids Surf. B *Biointerfaces* **2014**, 113, 176– 181.

18. M. A. Cameron, I. P. Gartland, J. A. Smith, S. F. Diaz, S. M. George, Atomic layer deposition of SiO_2 and TiO_2 in alumina tubular membranes: pore reduction and effect of surface species on gas transport, Langmuir 16, 19 (2000) 7435-744.

19. Romero, V.; Vega, V.; García, J.; Zierold, R.; Nielsch, K.; Prida, V.M.; Hernando, B.; Benavente, J. Changes in Morphology and Ionic Transport Induced by ALD SiO_2 Coating of Nanoporous Alumina Membranes. *ACS Appl. Mater. Interfaces* **2013**, 5, 3556-3564.

20. Skoog, S. A.; Elam, J. W.; Narayan, R. J. Atomic layer deposition: medical and biological applications; *International Materials Reviews* **2013**, 58, 113-129.

21. Vega, V.; Gelde, L.; González, A.S.; Prida, V. M.; Hernando, B.; Benavente, J. Diffusive transport through surface functionalized nanoporous alumina membranes by atomic layer deposition of metal oxides. *J. Ind. Eng. Chem.* **2017**, 52, 66–72.

22. Gelde, L.; Cuevas, A.L.; Martínez de Yuso, M. V.; Benavente, J.; Vega, V.; González, A. S.; Prida, V.M.; Hernando, B. Influence of TiO_2-Coating Layer on Nanoporous Alumina Membranes by ALD Technique; *Coatings* **2018**, 8, 60-72.

23. B. Ch. Mallick, Ch-T. Hsieh, K.-M. Yin, Y. A. Gandomi, K.-T. Huang, Review—On Atomic Layer Deposition: Current Progress and Future Challenges, *ECS J. Solid State Sci. Technol.* **2019**, 8, N55-N78.

24. Weber, M.; Julbe, A.; Ayral, A.; Miele, P.; Bechelany, M. Atomic Layer Deposition for Membranes: Basics, Challenges, and Opportunities; *Chem. Mater.* **2018**, 30, 7368−7390.

25. Spende, A.; Sobel, N.; Lukas, M.; Zierold, R.; Riedl, J.C.; Gura, L.; Schubert, I.; Montero Moreno, J.M.; Nielsch, K.; Stühn, B.; Hess, C.; Trautmann, C.; Toimil-Molares, M.E. TiO_2, SiO_2, and Al_2O_3 coated nanopores and nanotubes produced by ALD in etched ion-track membranes for transport measurements, *Nanotechnology* **2015**, 26, 335301.

26. Xifre-Perez, E.; Guaita-Esteruelas, S.; Baranowska, M.; Pallares, J.; Masana, L.; Marsal, L.F. In Vitro Biocompatibility of Surface-Modified Porous Alumina Particles for HepG2 Tumor Cells: Toward Early Diagnosis and Targeted Treatment. *ACS Appl. Mater. Interfaces* **2015**, 7, 18600–18608.

27. Vázquez, M.I.; Romero, V.; Benavente, J.; Romero, R.; Hierrezuelo, J.; López-Romero, J.M.; Contreras-Cáceres, R. Characterization and stability of a bioactivated alumina nanomembrane for application in flow devices; *Micropor. Mesopor. Mat.* **2016**, 226, 88-93.

28. Pol, L.; Eckstein, C.; Acosta, L.K.; Xifré-Pérez, E.; Ferré-Borrull, J.; Marsal, L.F. Real-Time Monitoring of Biotinylated Molecules Detection Dynamics in Nanoporous Anodic Alumina for Bio-Sensing. *Nanomaterials* **2019**, 9, 478.

29. E.S. Kooj, H. Wormeester, A.C. Galca, B. Poelsema, Optical Anisotropy and Porosity of Anodic Aluminum Oxide Characterized by Spectroscopic Ellipsometry. *Electrochem. Solid-State Lett, 6* (2003) B52-B54. https://doi.org/10.1149/1.1615351

30. Thompson, D.W.; Snyder, P.G.; Castro, L.; Yan, L.; Kaipa, P.; Woollam, J.A. Optical characterization of porous alumina from vacuum ultraviolet to midinfrared. *J. Appl. Phys.* **2005**, 97, 113511.

31. Law, C.S.; Lim, S.Y.; Abell, A.D.; Voelcker, N. H.; Santos, A. Nanoporous Anodic Alumina Photonic Crystals for Optical Chemo- and Biosensing: Fundamentals, Advances, and Perspectives. *Nanomaterials* **2018**, 8, 788.

32. Lim, S. Y.; Law, C. S.; Marsal, L. F.; Santos, A. Engineering of Hybrid Nanoporous Anodic Alumina Photonic Crystals by Heterogeneous Pulse Anodization, *Scientific Reports* **2018**, 8, 9455.

33. Brzózka, A.; Brudzisz, A.; Hnida, K.; Sulka, G. D. Chemical and Structural Modifications of Nanoporous Alumina and Its Optical Properties, in "Electrochemically Engineered Nanoporous Materials", D. Losic and A. Santos (eds.), Springer Series in Materials Science (**2015**) Chap. 8, pp. 219-288.

34. Meng, X.; Norouzi Banis, M.; Geng, D.; Li, X.; Zhang, Y.; Li, R.; Abou-Rachid, H.; Sun, X. Controllable atomic layer deposition of one-dimensional nanotubular TiO_2. *Appl. Surf. Sci.* **2013**, 266, 132–140.

35. Ariza, M.J.; Benavente, J.; Rodríguez-Castellón, E. The capability of X-ray Photoelectron Spectroscopy in the Characterization of Membranes: Correlation between Surface Chemical and Transport Properties in Polymeric Membranes. In *Handbook of Membrane Research: Properties, Performance and Applications*; Gorley, S.V., Ed.; Nova Science Publishers Inc.: New York, 2009, pp 257-290. ISBN: 978-1-60741-638-8.

36. Briggs, D.; Seah, M.P. *Practical Surface Analysis, 2nd ed. Vol I: Auger and X-ray photoelectron spectroscopy*; John Wiley & Sons: Chichester, 1995.

37. Cumpson, P.J. Angle-resolved XPS and AES: Depth-resolution limits and a general comparison of properties of depth-profile reconstruction methods. *J. Electron. Spectrosc. Relat. Phenom.* **1995**, 73, 25-52.

38. C. A. Schneider, W.S. Rasband, K.W. Eliceiri, NIH Image to ImageJ: 25 years of Image Analysis. *Nat. Methods* **2012**, 9, 671-675.

39. Romero, V.; Vázquez, M. I.; Benavente, J. Study of ionic and diffusive transport through a regenerated cellulose nanoporous membrane. *J. Membr. Sci.* **2013**, 433, 152-159.

40. Abramoff, M.D.; Magalhaes, P.J.; Ram, S.J. Image Processing with ImageJ. *Biophotonics Intern.* **2004**, 11, 36-42.

41. Moulder, J.F.; Stickl, W.F.; Sobol, P.E.; Bomben, K.D. in *Hand- book of X-Ray Photoelectron Spectroscopy*; Chastain, J., Ed.; Perkin-Elmer Corporation: Minneapolis, 1992.

42. NIST X-ray Photoelectron Spectroscopy (XPS) Database. https://srdata.nist.gov/xps/ (accessed Aug 20, 2019).

43. Swift, P. Adventitious carbon-the panacea for energy referencing. *Surf. & Interface Anal*. **1982**, 4, 47-51.

44. Keurentjes, J.T.F. ; Harbrecht, J.G.; Brinkman, D.; Hanemaaijer, J.H.; Cohen Stuart, M.A.; van't Riet, K. Hydrophobicity measurements of microfiltration and ultrafiltration membranes. *J. Membr. Sci*. **1989**, 47, 333-344.

45. Fortunato, R.; Afonso, C.A.M.; Benavente, J.; Rodriguez-Castellón, E.; Crespo, J.G. Stability of supported ionic liquid membranes as studied by X-ray photoelectron spectroscopy. *J. Membr. Sci.* **2005**, 256, 216-223.

46. Martesson, J.; Arwin, H.; Nygren, H.; Lundstrom I. Adsorption and optical properties of ferritin layers on gold studied with spectroscopic ellipsometry; *J. Colloid Interface Sci.* **1995**,174, 79-85.

47. Losurdo, M.; Begmair, M.; Bruno, G.; Cattelan, D.; Cobet, Ch.; De Martina, A.; Fleischer, K.; Dohcevic-Mitrovic, Z.; Esser, N.; Galliet, M.; Gajic, R.; Hemzal, D.; Hingeri, K.; Humlicek, J.; Ossikovski, R.; Popovic, Z.V.; Saxi; O. Spectroscopic ellipsometry and polarimetry for materials and systems analysis at the nanoscale: state-of-art, potential, and perspectives. *J. Nanopart. Res.* **2009**, 11, 1521-1554.

48. Ogieglo, W., Wormeerster, H., Wessling, M., & Benes, N. E., Spectroscopic ellipsometry analysis of a thin film composite membrane consisting of polysulfone on a porous αalumina support. *ACS Appl. Mater. Interfaces* **2012**, 4, 935–943.

49. Tompkins, G.; Hilfiker, J.N. Spectroscopic Ellipsometry: Practical Application to Thin Film Characterization, 1st ed.; Momentum Press: New York, NY, USA, 2016; pp. 57–70.

50. Zheng, H.; Zhang, R-J.; Li, D-H.; Chen, X.; Wang, S-Y.; Zheng, Y-X.; Li, M-J.; Hu, Z-G.; Dai, N.; Chen, L-Y. Optical properties of Al-doped ZnO films in the infrared region and their adsorption applications. *Nanoscale Res. Lett.* **2018**, 13, 149.

51. Cuevas, A. L.; Martínez de Yuso, M.V.; Vega, V.; González, A.S.; Prida, V.M.; Benavente, J. Influence of ALD coating layers on the optical properties of nanoporous alumina-based structures. *Coatings* **2019**, 9, 43-49.

52. Arman, I.S.; Rahman, Md.A.;. Ismail, A.B.Md. Electrical and morphological characterization of zinc-doped Fe_2O_3 thin films at different annealing temperature, *J. Mater. Res. Technol.* **2019**, 8, 5909-5915.

53. Sakai, N.; Ebina, Y.; Takada, K.; Sasaki, T. Electronic Band Structure of Titania Semiconductor Nanosheets Revealed by Electrochemical and Photoelectrochemical Studies. *J. Am. Chem. Soc.* **2004**, 126, 5851-5858.

54. Afanasév, V.V.; Houssa, M.; Stesmans, A.; Heyns, M.M. Bands alignements in metal-oxide-silicon structures with atomic layer deposited Al_2O_3 and ZrO_2. *J. Appl. Phys.* **2002**, 91, 3079.

55. Srikant, *V;* . Clarke. D. R. On the optical band gap of zinc oxide, *J. App. Phys.* **1998**, 83, 5447.

56. Sernelius, B.E.; Jin, Z.-C.; Hamberg, I.; Granqvist, C. G. Band-gap tailoring of ZnO by means of heavy Al doping, *Phys. Review B* **1988**, 3, 10244-10248.

57. Yuan, Z.; Wang, C.; Yi, X.; Ni, Z.; Chen, Y.; Li. T. Solid-State Nanopore. *Nanoscale Res. Lett.* **2018**, 13, 56.

58. Cuevas, A.; Campos, B.B.; Romero, R.; Algarra, M.; Vázquez, M.I.; Benavente, J. Eco-friendly Modification of a Regenerated Cellulose Based Film by Silicon, Carbon and N-doped Carbon Quantum Dots. *Carbohydr. Polym.* **2019**, 15, 238-244.

59. Kaspar, P.; Sobola, D.; Dallaev, R.; Ramazanov, S.; Nebojsa, A.; Rezaee, S.; Grmela; L. Characterization of Fe_2O_3 thin films on highly oriented pyrolytic graphite by AFM, ellipsometry and XPS, *Appl. Surf. Sci*. **2019**, 493, 673-678.

60. List of refractive index, 2020 www.vaxasoftware.com, (accessed May 14th 2020).

61. Marsal, L.F.; Vojkuvka, L.; Formentin, P.; Pallarés, J.; Ferré-Borrull, J. Fabrication and optical characterization of nanoporous alumina films annealed at different temperatures. *Optical Materials* **2008**, 31, 860-866.

62. Santos, A.; Macías, G.; Ferré-Borrull, J.; Pallarès, J.; Marsal. Ll. F. Photoluminescent Enzymatic Sensor Based on Nanoporous Anodic Alumina, *ACS Appl. Mater. Interfaces* **2012**, 4, 3584−3588.

63. Shang, G. L.; Fei, G. T.; Zhang, Y.; Yan, P.; Xu, S. H.; Zhang, L. D. Preparation of narrow photonic bandgaps located in the near infrared region and their applications in ethanol gas sensing, *J. Mater. Chem. C* **2013**, 1, 5285.

64. Law, C. S.; Lim, S. Y.; Abell, A. D.; Voelcker, N. H.; Santos. A. Nanoporous Anodic Alumina Photonic Crystals for Optical Chemo- and Biosensing: Fundamentals, Advances, and Perspectives, *Nanomaterials* **2018**, 8, 788.

65. Holbein, J.; Steinhart, M.; Schiene-Fisher, C.; Benda, A.; Hof, M.; Hübner, C.G. Confined diffusion in ordered nanoporous membranes. *Small* **2007**, 3, 380-385.

66. Jiang, X.; Mishra, N.; Turner, J.N.; Spencer, M.G. Diffusivity of sub-1,000 Da molecules in 40 nm silicon-based alumina pores. *Microfluid. Nanofluid.* **2008**, 5, 695-701.

67. Kipke, S.; Schmid, G. Nanoporous alumina membranes as diffusion controlling systems. *Adv. Funct. Mater.* **2014**, 14, 1184-1190.

68. Romero, V.; Vega, V.; García, J.; Prida, V.M.; Hernando, B.; Benavente, J.; Effect of Porosity and Concentration Polarization on Electrolyte Diffusive Transport Parameters through Ceramic Membranes with Similar Nanopore Size. *Nanomaterials* **2014**, 4, 700-711.

69. Mulder, M. *Basic Principles of Membrane Technology*; Kluwer Academic Publishers: Dordrecht 1992.

70. Lakshminarayanaiah, N. *Transport Phenomena in Membranes*; Academic Press: New York, 1969.

71. Meyer, K.H.; Sievers, J.F. La permeabilité des membranes I. Theorie de la permeabilité ionique. *Helv. Chim. Acta* **1936**, 19, 646-651.

72. Teorell, T. Transport phenomena in membranes. *Discuss. Faraday Soc.* **1956**, 21, 9-26.

73. Szymczyk, A.; Fievet, P.; Investigating transport properties of nanofiltration membranes by means of a steric, electric and dielectric exclusion model. *J. Membr. Sci.* **2005**, 252, 77-88.

74. Robinson, R.A.; Stokes, R.H. *Electrolyte Solutions*; Butterworths: London, 1970.

Supplementary Material

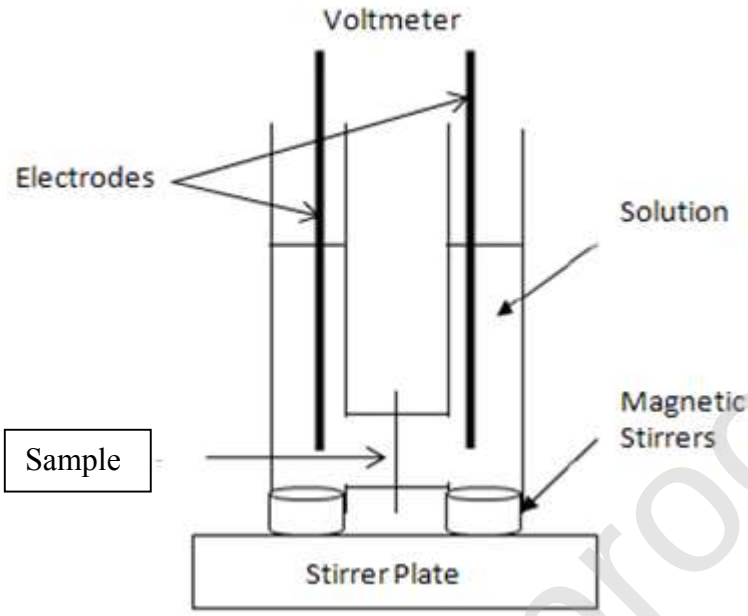

Fig. SI1: Scheme of electrochemical test-cell.

Table SI1: Average pore radii (<r_p>), effective fixed charge (X_f) and anionic permselectivity (P_{Cl^-}) for analysed samples.

Sample	**<r_p> (nm)**	**X_f (mol)**	**P_{Cl^-} (%)**
Ox	16 ± 2	+ 1.0×10^{-2}	40.8
Ox+Al_2O_3	12 ± 2	+ 1.3×10^{-2}	55.0
Ox+TiO_2	13 ± 2	+ 0.9×10^{-2}	28.3
Ox+Fe_2O_3	12 ± 1	+ 0.8×10^{-2}	20.5
Ox+ZnO	12 ± 2	+ 1.7×10^{-2}	48.8

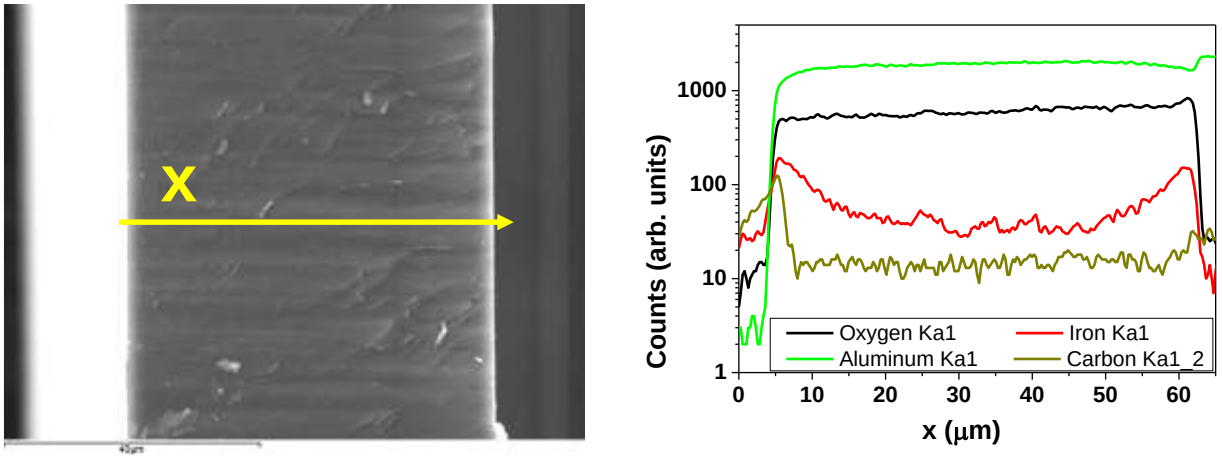

Fig. SI2: EDS composition profile obtained in a cross section of the NPAS+Fe_2O_3 sample, indicating the distribution of oxygen, aluminum, iron and carbon.

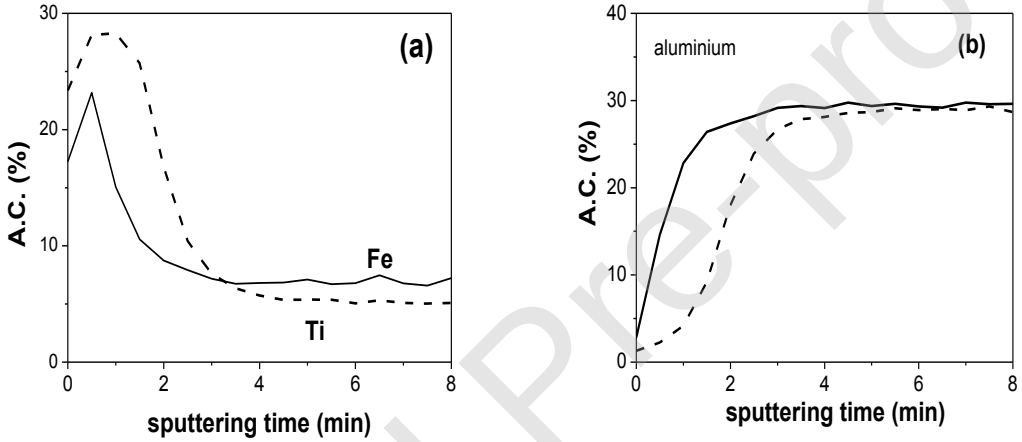

Fig. SI3: Comparison of atomic concentration % evolution with sputtering time for: (a) Fe (NPAS+Fe_2O_3 sample, dense line) and Ti (NPAS+TiO_2 sample, dashed line); (b) Al for NPAS+Fe_2O_3 (dense line) and NPAS+TiO_2 (dashed line) samples.

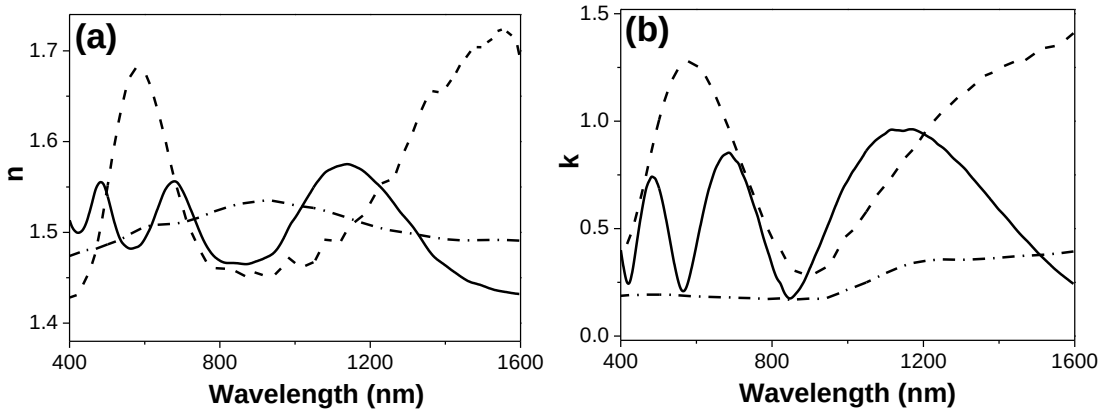

Fig. SI4: Comparison of wavelength dependence of: (a) refraction coefficient (n), and (b) extinction coefficient (k), for three aluminum anodized samples with different pore radii (r_p) and porosity (Θ). NPAS (r_p = 12 nm, Θ = 12%: solid line) NPAS* (r_p =23 nm, Θ = 17%: dashed line) and NPAS** (r_p = 110 nm, Θ = 20%: dashed-dotted line).

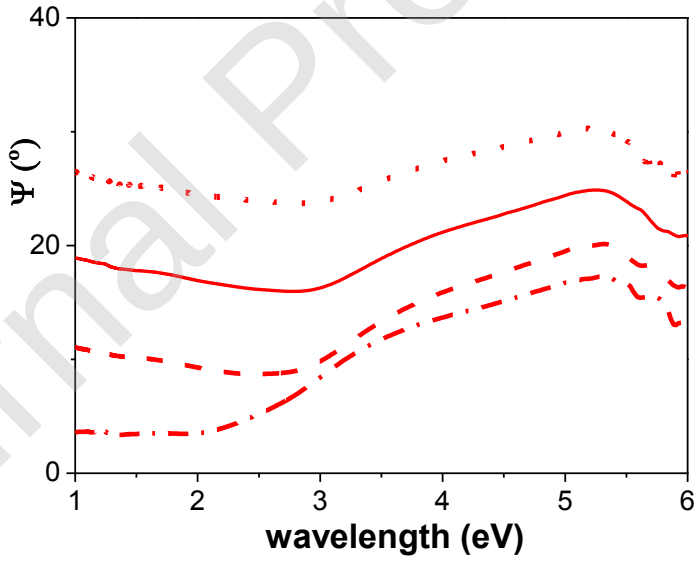

Fig. SI5: Wavelength dependence of the ellipsometry angle ψ measured at different light incident angles for the NPAS+Fe_2O_3 sample: 60º (dashed-dotted line), 65º (dashed line), 70º (solid line) and 75º (dotted line).

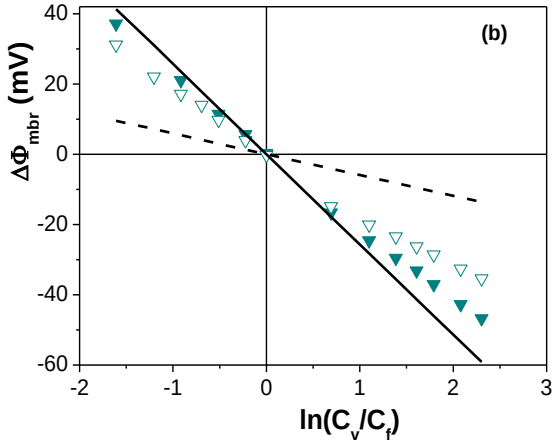

Fig. SI6. Comparison of membrane potential measurements as a function of the solute concentrations ratio (C_v/C_f) for samples NPAS+TiO_2 (pore radii 9 ± 2 nm, ▼) and NPAS*+TiO_2 (pore radii 13 ± 2 nm, ∇).